

See discussions, stats, and author profiles for this publication at: <https://www.researchgate.net/publication/8003337>

# Identification of B and T cells in human spleen sections by infrared microspectroscopic imaging

ARTICLE *in* CYTOMETRY PART A · APRIL 2005

Impact Factor: 2.93 · DOI: 10.1002/cyto.a.20117 · Source: PubMed

---

CITATIONS

26

---

READS

21

4 AUTHORS, INCLUDING:



**Christoph Krafft**

Institut für Photonische Technologien

**150** PUBLICATIONS **2,972** CITATIONS

SEE PROFILE



**Michael E Meyer-Hermann**

Helmholtz Centre for Infection Research

**111** PUBLICATIONS **1,402** CITATIONS

SEE PROFILE

---

Original Articles

---

# Identification of B and T Cells in Human Spleen Sections by Infrared Microspectroscopic Imaging

Christoph Krafft,<sup>1\*</sup> Reiner Salzer,<sup>1</sup> Gerhard Soff,<sup>2</sup> and Michael Meyer-Hermann<sup>3</sup>

<sup>1</sup>Institute for Analytical Chemistry, Dresden University of Technology, Dresden, Germany

<sup>2</sup>Institute for Theoretical Physics, Dresden University of Technology, Dresden, Germany

<sup>3</sup>Centre for Mathematical Biology, Mathematical Institute, Oxford, United Kingdom

Received 5 May 2004; Revision Received 27 August 2004; Accepted 16 December 2004

**Background:** Infrared spectroscopy probes the chemical composition and molecular structure of complex systems such as tissue and cells. Infrared spectroscopic imaging combines this spectral information with lateral resolution near the single-cell level. We analyzed whether this method is competitive with classic immunohistochemical methods for immunologic tissue and cells.

**Methods:** We recorded infrared microspectroscopic mapping datasets with a  $90 \times 90\text{-}\mu\text{m}^2$  aperture from a  $3 \times 3\text{-mm}^2$  unstained tissue area of human spleen. A secondary follicle containing a germinal center and a T zone were studied in more detail by infrared microspectroscopic imaging with lateral resolution near  $5\text{ }\mu\text{m}$ . The results were compared with consecutive sections stained by immunoglobulin D antibodies. T and B lymphocytes were extracted from human blood and served as independent test samples.

**Results:** Cluster analysis of infrared datasets produced images that distinguished anatomical features such as pri-

mary and secondary follicles, T zones, arteries, and spleen red pulp. The assignments could be confirmed in consecutive sections by immunohistochemical staining. Main spectral variances between T and B lymphocytes in high-resolution measurements were attributed to specific spectral contributions of DNA and cytosol.

**Conclusions:** Sensitivity and specificity of the infrared based methods are comparable to those of standard staining procedures for identification of B and T cells. However, infrared spectroscopic imaging can offer advantages in velocity, data throughput, and standardization because of minimal sample preparation. The results emphasize the potential of infrared spectroscopy as an innovative tool for the distinction of cell types, in particular in immunologic tissue. © 2005 Wiley-Liss, Inc.

**Key terms:** secondary lymphoid organs; lymphocyte identification; infrared spectroscopic imaging

Germinal centers (GCs) are important components of the adaptive immune response (1) that takes place in secondary lymphoid organs such as the spleen and tonsils. GCs are sites of intense somatic hypermutation and antigen-specific selection of B cells and are responsible for affinity maturation of B cells that have been activated with T-cell help. Within a GC reaction, antibody producing plasma cells and memory B cells are generated. The mechanisms driving the GC reaction have been frequently discussed. However, the underlying cell interaction processes, e.g., adhesion, chemotaxis, and affinity-dependent selection, remain an object of speculation (2–5). We previously showed in a theoretical approach the possibility of using simulations to disentangle cell interactions involved in GCs on the basis of morphologic considerations (6). This approach lacks a stable and statistically significant experimental data basis.

Standard procedures in immunology and molecular biology for identification of B and T cells are methods that detect variations in morphology, tissue architecture, staining patterns, or sensitivity to a number of specific anti-

---

Michael Meyer-Hermann's current address: Frankfurt Institute for Advanced Studies (FIAS), Johann Wolfgang Goethe-University, Max von Laue str. 1, 60438 Frankfurt am Main, Germany. E-mail: M. Meyer-Hermann@fias.uni-frankfurt.de

Contract grant sponsor: Marie Curie Intra-European Fellowship, Sixth EU Framework Program; Contract grant sponsor: Volkswagen Foundation.

\*Correspondence to: Christoph Krafft, Institute for Analytical Chemistry, Dresden University of Technology, 01062 Dresden, Germany.

E-mail: christoph.krafft@chemie.tu-dresden.de

Published online 23 February 2005 in Wiley InterScience (www.interscience.wiley.com).

DOI: 10.1002/cyto.a.20117

bodies. Although these methods are well established, they require extensive sample preparation. Spectroscopic methods provide additional and complementary pathways of analyses (7). Spectral data can be collected and interpreted by computer-based algorithms, which offer the possibility of objective and comparative analyses of different samples using the same mode of evaluation. Infrared (IR) spectroscopy is among the methods of vibrational spectroscopy, with promising potential as an analytical tool to assess tissues and cells because it can probe chemical compositions and compositional and structural changes in complex systems on the molecular level with minimal sample preparation. Previous investigations of tissue by IR spectroscopy include studies of breast (8), colon (9), cervical tissue (10), skin (11), oral mucosa (12), heart (13), liver (14), lung (15), and brain (16).

The application fields of IR spectroscopy have significantly increased since the coupling of focal plane array (FPA) detectors to Fourier transform IR (FTIR) spectrometers (17). This method combines the instrumental multiplex advantage of the Michelson interferometric Fourier transform technique with the multichannel advantage of an imaging system. Specifically, the multiple detector elements enable spectra at all pixels to be collected simultaneously, and the interferometer portion of the system allows all spectral features to be measured concurrently. Further, using a FTIR spectrometer coupled to a microscope and a FPA detector enables the acquisition of thousands of spectra within minutes with diffraction limited spatial resolution of the order of single cells. These unique features extend IR spectroscopic applications. Initial studies have been reported for visualization of silicone gel in breast tissue (18) and for imaging collagen and proteoglycan in cartilage (19,20).

In this report we use data acquisition techniques based on IR spectroscopy in the context of immunologic tissue and cells that offer advantages in velocity, higher data throughput, standardization, and in this way to better statistics than traditional techniques, e.g., immunohistologic staining procedures. To this end, consecutive sections of human spleen were analyzed by both methods. First, immunoglobulin D (IgD) antibodies were used as markers for follicles and T zones on a thin section. Then these areas were identified on the neighboring section by using IR mapping with an aperture of  $90 \times 90 \mu\text{m}^2$ . In addition, follicles and T zones were analyzed in more detail using IR imaging with diffraction-limited high resolution near  $5 \mu\text{m}$ . Cluster algorithms were applied for image reconstruction. T and B lymphocytes were extracted from human blood by specific antibodies. IR images were recorded from these cells as independent test samples and the spectral features were compared with results from spleen tissue. The cell identification potential of these techniques is discussed.

## MATERIALS AND METHODS

### Tissue Preparation

A spleen sample from a 17-year-old man was frozen in liquid nitrogen immediately after surgery without fixatives

and antifreeze medium. Because unstained tissue sections cannot be studied easily in visible microscopy and the stains used for normal visual microscopy have distinct IR spectra that interfere with tissue signals, we prepared two sets of consecutive sections by a cryotome. First, four  $10\text{-}\mu\text{m}$  tissue sections were transferred onto a glass slide and stained for IgD (21). Second, four  $10\text{-}\mu\text{m}$  tissue sections were transferred onto an IR transparent calcium fluoride slide and air dried for IR spectroscopy.

### Immunomagnetic Isolation of B and T Cells

A blood sample was obtained from a healthy donor who gave informed consent. Peripheral blood mononuclear cells were prepared by Ficoll-Hypaque (Biochrom, Berlin, Germany) density centrifugation. Antibodies CD3 and CD19 were specific for T cells and B cells, respectively. CD3-positive T cells and CD19-positive B cells were isolated from peripheral blood mononuclear cells using immunomagnetic separation (Miltenyi Biotec, Bergisch-Gladbach, Germany) according to the manufacturer's instructions. The purities of the isolated T and B cells were 95% and 85%, respectively, as assessed by flow cytometric analysis. The suspensions contained approximately  $8 \times 10^5$  T cells and  $1.1 \times 10^6$  B cells in phosphate buffered saline. For IR spectroscopy, cells were pelleted by centrifugation, resuspended in  $15 \mu\text{l}$  of phosphate buffered saline, transferred on a calcium fluoride slide, and air dried.

### Data Collection

IR microspectroscopic maps were collected in transmission mode by using a FTIR spectrometer with a single detector element and an adjustable microscope aperture to select an area from which to obtain spectral data. Subsequently, the sample was moved by a motorized stage in a raster pattern in increments of the same size as the optical aperture. Before data acquisition, a grid was defined on the tissue section, with each grid square corresponding to an area of  $90 \times 90 \mu\text{m}^2$ . A FTIR spectrometer (IFS66/S, Bruker Optik, Ettlingen, Germany) equipped with an IR microscope (IR-Scope, Bruker), a motorized stage, and a liquid nitrogen-cooled mercury cadmium telluride detector were used. The microscope and the FTIR spectrometer were continually purged by dry air from air purifiers. The microscope was enclosed in a plastic box to provide good purging. Five scans at  $4\text{-cm}^{-1}$  resolution were collected and Fourier transformed to produce the resulting spectrum from  $950$  to  $3,800 \text{ cm}^{-1}$ . After every 40 sample spectra, a new background spectrum was recorded. Data acquisition by the Bruker software OPUS and moving of the stage in increments of  $90 \mu\text{m}$  were controlled by in-house software. Approximately 10 spectra were recorded per minute, so the total acquisition time for a  $35 \times 35$  map of 1,225 spectra was approximately 2 h.

IR spectroscopic images were collected in transmission mode by using a FTIR spectrometer with a FPA detector. The size of each FPA pixel and the magnification of the optional microscope determine the spatial resolution, which is limited by diffraction. The total area from which

spectra are recorded without moving the sample depends on the dimension of the FPA detector. For our experiments, the FTIR spectrometer was coupled to the microscope Bruker Hyperion with 15-fold magnification that was connected to a  $64 \times 64$  mercury cadmium telluride-based FPA with a total area of  $4 \times 4 \text{ mm}^2$ . This results in a detectable area under the microscope of  $266 \times 266 \mu\text{m}^2$  with a calculated (apparent) resolution of  $4.2 \mu\text{m}/\text{pixel}$ . Compared with IR mapping, accumulation times of the IR imaging technique are decreased approximately 50-fold. Acquisition of a  $64 \times 64$  image consisting of 4,096 spectra with  $8\text{-cm}^{-1}$  spectral resolution, 40 coadditions, and 40-ms stabilization delay requires just 8 min. When the microscopic sampling area exceeded  $266 \times 266 \mu\text{m}^2$ , after image acquisition the sample stage was moved in increments of  $266 \mu\text{m}$  to the next position, which was controlled by in-house software. After every four sample images, a new background image was recorded and averaged to compensate for small fluctuations in the environment.

### Data Treatment

IR mapping and imaging datasets were imported into MatLab (The Mathworks Inc., Natick, MA, USA). Data pretreatment included filtering, baseline correction, and normalization. Spectra with extreme values, e.g., amide I absorbances below 0.1 or above 1, were removed from the datasets so that errors due to holes in the tissue sections, saturation effects, nontissue impurities, or dead pixels of the FPA detector were avoided. Then a straight baseline was subtracted, which incorporated two minima near  $950$  and  $1,800 \text{ cm}^{-1}$ . This procedure eliminates different spectral offsets without losing relevant background information. An additional baseline point near  $1,150 \text{ cm}^{-1}$  was inserted for IR spectra from IR imaging, and the spectral region  $950$  to  $1,150 \text{ cm}^{-1}$  was not considered for analysis because some spectra showed unusual background features below  $1,150 \text{ cm}^{-1}$  due to decreased transmission of calcium fluoride window material. Spectra were normalized to an amide I intensity equal to 1, which compensates different sample thickness. The amide I band

near  $1,650 \text{ cm}^{-1}$ , which is assigned to proteins, is usually the most intense band in IR spectra from tissue, with only minor spectral contributions from other constituents such as lipids or nucleic acids. Individual spectra were analyzed with Grams32 (Thermo Galactic, Salem, NH, USA).

### Cluster Analysis

In general, cluster analysis identifies regions of the sample that have a similar spectral response by clustering the spectra into groups or clusters such that differences in intracenter spectral responses are minimized and inter-center differences between spectral responses are maximized. The results of a cluster analysis include, for each cluster, the cluster centroid spectrum (weighted mean spectrum for the cluster) and the corresponding cluster membership map (spatial distribution of the cluster). Taken together, cluster analysis answers two commonly posed questions: Where did the different types of spectra occur (shown by cluster membership maps)? and What were the spectral characteristics (depicted by cluster centroids)?

The unsupervised classification method k-means cluster analysis was performed because it can handle a large amount of data as obtained during IR imaging experiments. The N k-means algorithm, which was implemented in the Matlab environment, was modified to incorporate a Euclidian distance metric, a random cluster initialization scheme, and data normalization. The algorithm was initiated by choosing the number of clusters. The criterion used to determine the number of clusters to be included in the analysis was that the clusters could be related to histologically distinct areas in the tissue sections. The initial spectra for the centers of these clusters were taken randomly from the spectral dataset. All spectra in the dataset were then compared with these cluster centers and assigned to the center that they most resembled. After assigning all spectra to one of the clusters, the new cluster center was calculated by taking the mean of all the spectra that were assigned to that cluster. This procedure was repeated until a stable solution was reached. The cluster

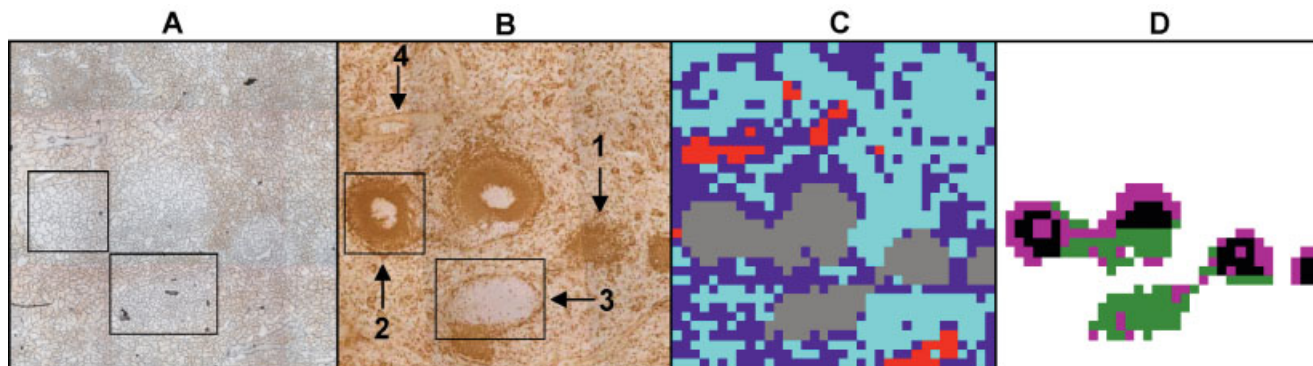


FIG. 1. **A:** Photomicrograph of a  $3.15 \times 3.15\text{-mm}^2$  dried section of spleen tissue. **B:** Photomicrograph of a consecutive tissue section stained by IgD antibodies. Color-coded plots are based on cluster analysis of all IR spectra in an IR mapping dataset (**C**) and on cluster analysis of IR spectra identified as B- and T-cell-rich areas (**D**). [Color figure can be viewed in the online issue, which is available at [www.interscience.wiley.com](http://www.interscience.wiley.com).]

membership information was plotted as a pseudocolor map by assigning a color to each different cluster.

## RESULTS

Figure 1A shows a photomicrograph of a dried, unstained section of a human spleen. Figure 1B shows the consecutive section, which was immunohistologically stained by IgD antibodies. Follicles containing mostly naive B cells can be identified by IgD-positive staining (arrow 1). In addition, secondary follicles containing a GC, a broad IgD-positive corona around a white IgD-negative area in the center, can be identified (arrow 2). The GCs consist of a melange of cells, in particular of B cells in different stages of differentiation. In the outer region of secondary follicles, the marginal zone can be identified as a slightly lighter IgD-positive area. T zones are characterized by a IgD-negative area surrounded by a thin ring of IgD-positive B cells (arrow 3). Some arteries and splenic trabeculae (arrow 4) can be distinguished in the mostly IgD-negative red pulp surrounding the follicles.

Figure 1C shows the same tissue area as Figure 1A digitally stained by IR mapping. A grid of  $35 \times 35$  pixels was defined for IR mapping to record spectra from a  $3.15 \times 3.15\text{-mm}^2$  area. The spectral dataset was analyzed by cluster analysis in the spectral range of  $950$  to  $1,800\text{ cm}^{-1}$ , and the processed data were reassembled into a color-scaled image. Four clusters are plotted against the coordinates of the spectral element. Comparison of Figures 1B and 1C shows that red pulp in spleen is represented by

cyan and blue clusters, and arteries and splenic trabeculae are indicated by the red cluster. Interestingly, the follicles and T zones, i.e., those areas dominated by B and T cells, are clearly distinguished from other spleen tissue by cluster analysis (gray cluster).

A second cluster analysis in the spectral range of  $950$  to  $1,800\text{ cm}^{-1}$  was performed with only B and T cells (gray cluster) as input. Figure 1D shows the resulting three clusters. We find a separation of T cells (green cluster) from two classes of B-cell-rich areas, which may be attributed to primary follicles (black) and the corona (black) surrounding GCs and to marginal zones of secondary follicles (magenta). Consistent with the fact that GCs contain different cell types, the GCs appear as black or as magenta clusters. These findings can be interpreted as an identification of T cells and two classes of B cells by IR spectra, which differ in their general properties and which correspond to the dominant cell type in the zones.

Because the cluster analysis method yielded characteristic spectra with significant signatures that can be correlated with results from immunohistologic staining, it is interesting to compare these spectra. Figure 2A shows typical IR spectra in the spectral range of  $950$  to  $1,800\text{ cm}^{-1}$ , representing red pulp (trace 1, blue cluster; trace 2, cyan cluster), arteries and splenic trabeculae (trace 3, red cluster) from Figure 1C, and Figure 2B shows typical IR spectra representing T cells (trace 6, green cluster) and B cells (trace 5, magenta cluster; trace 4, black cluster) from Figure 1D. The spectra were baseline

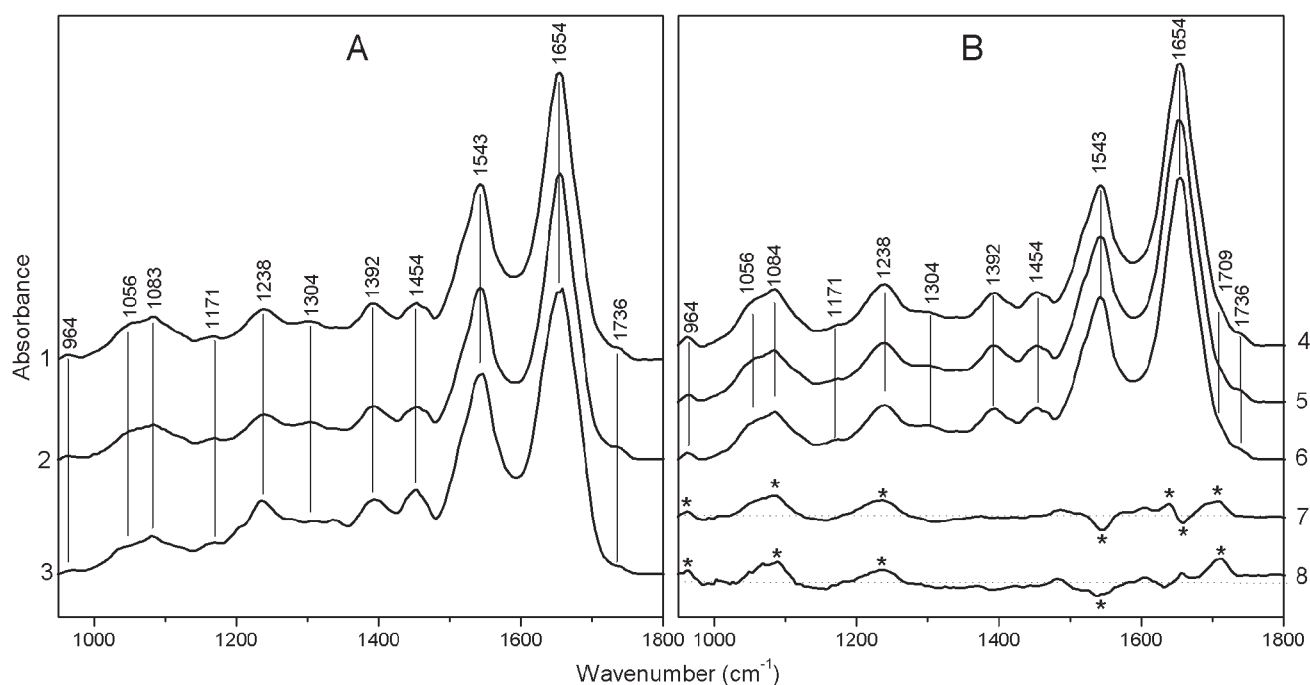


FIG. 2. Infrared spectra from  $950$  to  $1,800\text{ cm}^{-1}$  representing clusters from the mapping data set in Figures 1C (A) and 1D (B). Trace 1, red pulp (blue cluster); trace 2, red pulp (cyan cluster); trace 3, arteries (red cluster); trace 4, germinal center and corona B cells (black cluster); trace 5, marginal zone B cells (magenta cluster); trace 6, T cells (green cluster); trace 7, difference spectrum (trace 4 – trace 2); trace 8, threefold-amplified difference spectrum (trace 4 – trace 5). For presentation, all spectra were baseline corrected, normalized, and shifted to avoid overlapping.



corrected and normalized as described in Materials and Methods. All spectra exhibit bands near 1,171, 1,304 (amide III), 1,392 ( $\text{COO}^-$ ), 1,454 ( $\text{CH}_2/\text{CH}_3$  deformation), 1,543 (amide II), and 1,654  $\text{cm}^{-1}$  (amide I), which are characteristic of proteins as the main tissue constituent. The amide bands arise from vibrations of the amide groups comprising the peptide linkages of proteins. Additional bands near 964, 1,056, 1,083/1,238 (symmetric/antisymmetric stretching vibrations of phosphodioxo groups  $\text{PO}_2$ ), and 1,736  $\text{cm}^{-1}$  (carbonyl  $\text{C}=\text{O}$  of ester groups) can be assigned to lipids and nucleic acids. Differences that are diagnostic for the tissue types can be identified as, e.g., wavenumber shifts, changes in relative intensities, bandwidths, or baseline slopes.

The two spectra representing red pulp (Fig. 2A, traces 1, 2) show only minor differences. The presence of two distinct clusters is consistent with slight variations in color of Figure 1A. The raw spectra of arteries (Fig. 2A, trace 3) showed the highest absorbances before normalization and anomalous dispersion effects that are reflected as irregularities in the amide I band shape. Compared with the spectra from red pulp, the normalized spectra of the arteries are characterized by decreased bands near 1,080  $\text{cm}^{-1}$  and by increased bands near 1,238, 1,454, and 1,543  $\text{cm}^{-1}$ .

When compared with spectra from red pulp in Figure 2A, bands near 964, 1,056, 1,085, 1,238  $\text{cm}^{-1}$  and a shoulder near 1,709  $\text{cm}^{-1}$  were increased in spectra of B- and T-cell-dominated areas in Figure 2B, with maximum intensities for GC and corona B cells (trace 4). A difference spectrum between spectra of the corona and the red pulp (trace 7 = trace 4 – trace 2) and a difference spectrum of corona and marginal zone (trace 8 = trace 4 – trace 5) were included in Figure 2B for better visualization of the observed spectral changes. Because the intensities of the difference spectrum in trace 8 were approximately three times weaker than the intensities of the difference spectrum in trace 7, it was amplified three-fold for comparison. After this normalization, both difference spectra showed similar features. From the absence of significant difference bands for alkyl  $\text{CH}_2$  groups, we concluded that the positive difference bands at 1,085 and 1,238  $\text{cm}^{-1}$  could be assigned to phosphodioxo groups of nucleic acids rather than of phospholipids. The presence of positive difference bands near 964 and 1,709  $\text{cm}^{-1}$ , which also belongs to prominent bands in nucleic acid spectra, supports the conclusion. This increase of DNA bands points to increased cell density, i.e., less cytoplasm and increased nucleic acid concentration per surface area, or to DNA synthesis, i.e., to more proliferative activity and a nucleus in a less condensed state (14).

Differences were also found near the amide bands in both difference spectra. The negative difference band near 1,540  $\text{cm}^{-1}$  can be assigned to the amide II band, and positive and negative difference bands near 1,650/1,660  $\text{cm}^{-1}$  to the amide I band. This indicates that, aside from nucleic acids, there were alterations in the protein component that were characteristic of the tissue type.

For IR spectroscopic imaging, the secondary follicle marked in Figures 1A and 1B (arrow 2) was selected. Because the size of the area was approximately  $800 \times 800 \mu\text{m}^2$ , recording of nine  $266 \times 266 \mu\text{m}^2$  images was required for complete coverage. Due to a higher spatial resolution near 5  $\mu\text{m}$ , more details in the range of the single-cell level could be resolved. In contrast to 1,225 spectra of the mapping dataset analyzed in Figure 1, pooling of nine IR images led to a dataset with 36,864 spectra. A cluster analysis of the pooled imaging datasets was performed by using the spectral range of 1,150 to 1,800  $\text{cm}^{-1}$ . Similar to the results from IR mapping, this results in four clusters shown in Figure 3A: red pulp (orange cluster), follicles (blue cluster), and features that correlate with cracks throughout the sample (green and red clusters). White spots in the upper corners of individual IR images indicate dead pixels due to detector delamination.

For improved separation of corona B cells and marginal zone B cells, a second cluster analysis was performed from 1,150 to 1,800  $\text{cm}^{-1}$  with the blue follicle cluster as input. The result presented in Figure 3B shows that the red and yellow clusters form an inner ring, which correlates with naive B cells in the corona of the GC. The spectra of the blue cluster forms an outside ring that correlates with the light IgD positive area in Figure 1B that can be identified as the marginal zone.

The T zone marked in Figures 1A and 1B (arrow 3) was selected for the second IR spectroscopic imaging. Because the size of the area was approximately  $1,060 \times 800 \mu\text{m}^2$ , recording of 12  $266 \times 266 \mu\text{m}^2$  images was required for complete coverage, resulting in a pooled dataset of 49,152 spectra. Two cluster analyses were performed by using the spectral range of 1,150 to 1,800  $\text{cm}^{-1}$ . Analogous to Figure 3A, the first analysis included all spectra and revealed four clusters in Figure 3C that represented red pulp (orange), cracks (green and red), and B and T cells (blue). In the next step, the spectra representing cracks were removed from the dataset. A second cluster analysis was performed with only the spectra of T zone (blue) and red pulp (orange) from Figure 3C as input. This resulted in three clusters in Figure 3D, with improved separation of cells in the T zone (yellow) from cells in the surrounding tissue (blue). The borderzone is better defined and less tissue spectra (blue) are visible in the T zone (yellow) and vice versa. IR spectra, which are not assigned to red pulp or T zone, are represented by the red cluster and are distributed throughout the dataset.

Figure 4 shows typical IR spectra in the spectral range of 950 to 1,800  $\text{cm}^{-1}$  extracted from the imaging dataset representing clusters from Figure 3A. Analogous to the spectral features of red pulp and of follicles in Figure 2, the IR spectrum of spleen red pulp (Fig. 4, trace 1) was dominated by protein bands, whereas the intensities of phosphodioxo bands were maximal in the IR spectrum of follicles (Fig. 4, trace 3). The fact that all nucleic acid and protein features found by IR mapping (Fig. 2, traces 7 and 8) were conserved in the difference spectrum of follicles minus red pulp (Fig. 4, trace 4 = trace 3 – trace 1)

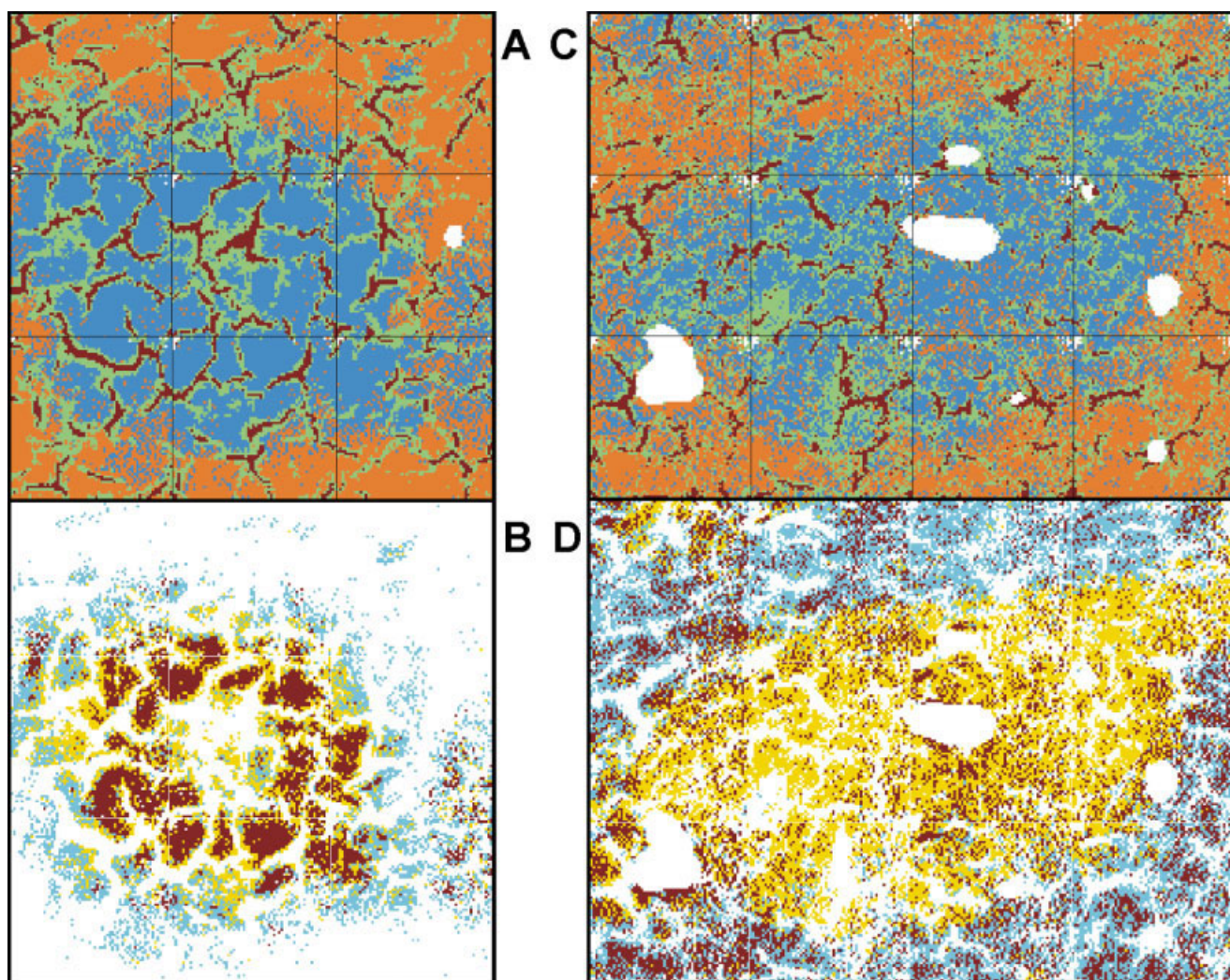


Fig. 3. IR spectroscopic imaging of secondary follicle in a  $800 \times 800\text{-}\mu\text{m}^2$  section (arrow 2 in Fig. 1B) and of a T zone in a  $1,060 \times 800\text{-}\mu\text{m}^2$  section (arrow 3 in Fig. 1B). Color-scaled plots are based on cluster analysis of all IR spectra (A, C), cluster analysis of IR spectra identified as B- and T-cell-rich areas (B), and cluster analysis of IR spectra after removal of cracks (D). [Color figure can be viewed in the online issue, which is available at [www.interscience.wiley.com](http://www.interscience.wiley.com).]

demonstrates their significance and reproducibility. They were marked by asterisks near  $964$ ,  $1,083$ ,  $1,238$ ,  $1,543$ ,  $1,650$ ,  $1,660$ , and  $1,709\text{ cm}^{-1}$ . A second difference spectrum of spectra from naive B cells in the corona (inner ring in Fig. 3B, red cluster) minus spectra from marginal zone B cells (outer ring in Fig. 3B, blue cluster) was amplified threefold for comparison in Figure 4, trace 5. Despite the decreased signal-to-noise ratio, the main difference features near  $1,240$ ,  $1,540$ , and  $1,710\text{ cm}^{-1}$  could be identified as in the other difference spectra (Fig. 2, traces 7 and 8; Fig. 4, trace 4). The absence of the positive difference bands near  $964$  and  $1,080\text{ cm}^{-1}$  can also be explained by the unusual background features in the spectral region of  $950$  to  $1,150\text{ cm}^{-1}$ , as attributed in Materials and Methods to the window material calcium fluoride. The difference spectrum in Figure 4, trace 5 corresponds to the black-minus-magenta difference spectrum in Figure

2B, trace 8, both representing the relation of naive B cells in corona and marginal zone B cells. Therefore, they should show similar features, which is the case. The important scale invariance of the results improves the credibility of the interpretation of the IR spectra from single-channel and FPA detectors and of the identification of clusters with specific cell properties.

Figure 4, trace 2 represents the IR spectrum of the crack (red cluster in Fig. 3A), which had no counterpart in Figure 2, because cracks were not resolved with the  $90 \times 90\text{-}\mu\text{m}^2$  aperture. The raw spectra of the cracks had the lowest absorbances. The normalized crack spectra show increased slopes in the range of  $1,150$  to  $1,800\text{ cm}^{-1}$ , increased intensity near  $1,056\text{ cm}^{-1}$ , and shifts of the amide I and amide II bands toward lower wavenumbers. The spectral properties of the second crack cluster (green in Fig. 3A, IR spectrum not shown) are between the



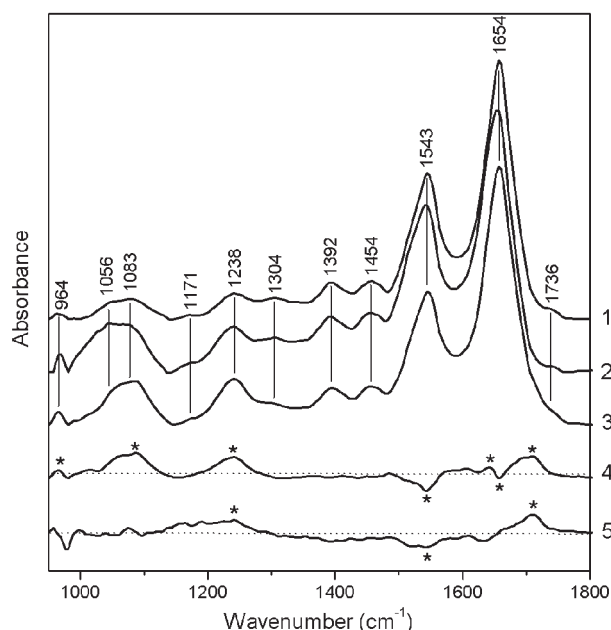


FIG. 4. IR spectra from 950 to 1,800  $\text{cm}^{-1}$  representing clusters from imaging datasets of secondary follicle. Trace 1, red pulp (orange cluster in Fig. 3A); trace 2, crack (red cluster in Fig. 3A); trace 3, GC and corona B cells (red cluster in Fig. 3B); trace 4, difference spectrum (trace 3 - trace 1); trace 5, threefold-amplified difference spectrum of GC and corona B cells (trace 3) minus marginal zone B cells (blue cluster in Fig. 3B, spectrum not shown).

spectra of the first crack and the red pulp. Therefore, we conclude that the depth of the crack correlates with the intensities of their spectral properties and that cracks represented by the green cluster are less deep than those represented by the red cluster. The minimum width of the cracks in Figures 3A and 3C could be estimated to be one pixel, i.e., 5  $\mu\text{m}$ . This observation demonstrated the high spatial resolution of the IR imaging method.

To verify that the measured spectral properties are related to specific cell properties, IR spectroscopic images were recorded from dried B and T cells that were extracted from human blood as described in Materials and Methods.  $\text{CD3}^+$  T cells comprise  $\text{CD4}^+$  and  $\text{CD8}^+$  and doubly negative T cells.  $\text{CD19}^+$  B cells include at least naive and memory B cells. Naive B cells in peripheral blood should show IR spectral properties similar to those of naive B cells in the corona of GC. However, the properties of other than naive B cells not necessarily correlate to those of B cells in the marginal zone but should express a lower DNA signal than naive B cells.

Cluster analyses of IR spectroscopic images showed two distinct classes of IR spectra in isolated B cells, whereas all IR spectra in isolated T cells were virtually the same. Figure 5 compares the cluster-averaged IR spectra of B cells (traces 1 and 2) and T cells (trace 3). The spectral signatures are similar to those for B and T cells from spleen (Figs. 2 and 4). Difference spectra were calculated for inspection of variances between B-cell clusters (trace 4 = trace 1 - trace 2) and B and T cells (trace 5 =

trace 2 - trace 3). Difference bands could be assigned to DNA bands near 964, 1,086, and 1,241  $\text{cm}^{-1}$  and to amide bands near 1,540 and 1,652  $\text{cm}^{-1}$ . A shift of the amide I band toward lower wavenumbers in trace 1 caused the strong difference feature that overlapped with the expected positive difference band near 1,709  $\text{cm}^{-1}$ , which was resolved in Figures 2 and 4. Positive difference bands indicating an increase of DNA bands in B cells from blood coincide with the results of naive B cells from spleen follicles in Figures 2 and 4. Thus, spectrum Figure 5, trace 1 with maximum spectral contribution of DNA corresponds to one of the naive B cells in spleen. Figure 5, trace 2 is attributed to IgD-negative memory and other B cells and mostly correspond to the spectrum of marginal zone B cells. This spectrum shows only a small increase of DNA bands compared with T cells (Fig. 5, trace 3). Despite decreased amplitudes, the key difference bands that were marked by asterisks could also be identified in Figure 5, trace 5.

In summary, the spectral properties of B and T lymphocytes in peripheral blood show features similar to those found for specific compartments in spleen tissue. This supports the interpretation that the IR spectral properties seen in spleen tissue can be attributed to the lymphocyte subclasses that dominate the investigated compartments within the spleen.

## DISCUSSION

We have applied IR spectroscopic mapping and imaging methods to tissue from the spleen, i.e., a secondary lymphoid organ, and to lymphocytes from peripheral

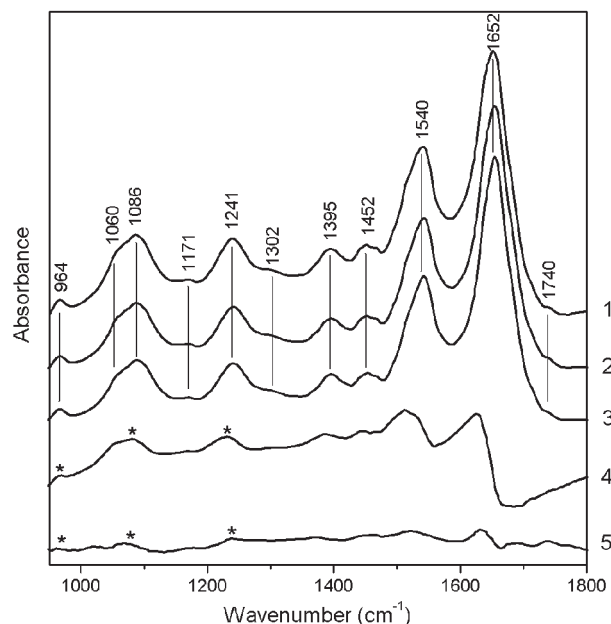


FIG. 5. IR spectra from 950 to 1,800  $\text{cm}^{-1}$  of B and T cells extracted from blood. Trace 1, B cells (class 1); trace 2, B cells (class 2); trace 3, T cells; trace 4, threefold-amplified difference spectrum (trace 1 - trace 2); trace 5, threefold-amplified difference spectrum (trace 2 - trace 3).



blood. Secondary lymphoid organs are specifically organized in compartments that are characterized by the domination of well-known cell types. Therefore, the crucial question was whether these methods can detect specific differences in lymphocytes. Identification of T and B cells in particular in different stages of differentiation is an important task in immunology. A main result of this study is that those compartments were similarly identified by IgD staining, CD3 and CD19 antibodies, IR mapping, and IR imaging. IR spectra contain specific information about proteins and nucleic acids that can be used for the differentiation of spleen red pulp, arteries, and B and T cells. Cluster analysis can be used for differentiation and classification of the IR spectra representing these types of tissue or cells. This identification was reproduced with the same accuracy using consecutive slices of the same organ (data not shown). The higher resolution IR imaging allows analysis of slices on a scale that is comparable to typical lymphocyte radii.

A more detailed analysis of the spectra showed that the cluster analysis grouped cells with interpretable specific molecular properties. This especially concerns the IR absorption of bands connected to nucleic acid density. In the present context, cells with large amounts of cytoplasm are plasma cells (present at different sites within follicles) and marginal zone B cells. Naive B cells in the corona are characterized by lower amounts of cytoplasm and, hence, by a larger surface fraction of nuclei (22). Therefore, we expect a domination of small nucleic acid absorption spectra in the outer region of the follicle and of large absorption in the inner region, especially in the corona, and this is what we have found: The IR spectra of the corona showed the most intense signal for nucleic acids compared with IR spectra that have been attributed to the marginal zone B cells. Moreover, GCs host B cells in different stages of differentiation, which is also reflected in different densities and fraction of nucleic acids. This result was equally found for the spectra taken at large and small scales, i.e., for IR mapping and IR imaging and for B and T cells of different origin, i.e., spleen and blood. The cluster analysis of IR spectra turns out to provide scale-invariant results at least concerning the nucleic acid absorption of the tissue. More generally, we found that, aside from nucleic acids, there were alterations in the protein component that are characteristic of the tissue type and should be established further.

The next tasks are to prepare tissue without cracks (Fig. 1A) and to resolve the outside ring around the T zone (Fig. 1B arrow 3) comprising IgD-positive B cells. These cells were not identified by this analysis because of the apparently smaller density of IgD-positive cells and because the spectral features diagnostic of T and B cells were less pronounced than those of different kinds of B cells shown in Figures 4 and 5. Improvements include acquisition of data with better signal-to-noise ratio and extension of the accessible spectral range. The first point can be achieved by modifying the IR imaging setup from a step-scan mode to a continuous-scan mode. The second point can be achieved by transferring the tissue sections on

barium fluoride windows, which offer better transmission than calcium fluoride windows, in particular for the low wavenumber region of 950 to 1,150  $\text{cm}^{-1}$ .

The GCs in the studied tissue section of a 17-year-old man have to be considered as nonactive GCs. Therefore, we could not expect a distinction of dark from light zones inside active GCs, which are dominated by proliferating and nonproliferating B cells, respectively. As a consequence of the presented results, a differentiation between these types of B cells in appropriate tissue should easily be accomplished based on the intensity of nucleic acid bands. Similarly, we previously demonstrated by IR spectroscopy that nonproliferating brain tissue has significantly less intense nucleic acid bands than do proliferating cultured brain cells (23).

## ACKNOWLEDGMENTS

We thank Birte Steiniger (University Marburg) for providing the stained and unstained slices of human spleen and for very enlightening and fruitful discussions. We thank Marc Schmitz (Dresden University of Technology) for providing B and T lymphocytes from blood. We are indebted to Joerg Galle and Hans Binder (University Leipzig) who encouraged this work. Michael Meyer-Hermann was supported by a Marie Curie Intra-European Fellowship within the Sixth EU Framework Program. Christoph Krafft was supported by the Volkswagen Foundation.

## LITERATURE CITED

1. MacLennan IC. Germinal centers. *Annu Rev Immunol* 1994;12:117-139.
2. Komai-Koma M, Donachie AM, Wildinson PC. Antigen-specific chemotaxis of B cells. *Immunology* 1997;91:579-585.
3. Ansel KM, Ngo VN, Hyman PL, Luther SA, Forster R, Sedgwick JD, Browning JL, Lipp M, Cyster JG. A chemokine-driven positive feedback loop organizes lymphoid follicles. *Nature* 2000;406:309-314.
4. Dubois B, Massacrier C, Caux C. Selective attraction of naive and memory B cells by dendritic cells. *J Leukoc Biol* 2001;70:633-641.
5. Guzman-Rojas L, Sims-Mourtada JC, Rangel R, Martinez-Valdez H. Life and death within germinal centres: a double-edged sword. *Immunology* 2002;107:167-175.
6. Meyer-Hermann M. A mathematical model for the germinal center morphology and affinity maturation. *J Theor Biol* 2002;216:273-300.
7. Martijn AN, Kraal G, Mebius RE. Effects on fluorescent and non fluorescent tracing methods on lymphocyte migration in vivo. *Cytometry* 2004;61A:35-44.
8. Fabian H, Jackson M, Murphy L, Watson PH, Fichtner I, Mantsch HH. Comparative infrared spectroscopic study of human breast tumors and breast tumor cell xenografts. *Biospectroscopy* 1995;1:37-45.
9. Lasch P, Wäsche W, McCarthy WJ, Müller G, Naumann G. Imaging of human colon carcinoma thin sections by FT-IR microspectroscopy. *Proc SPIE* 1998;3257:187-198.
10. Chiriboga L, Xie P, Vigorita V, Zarou D, Zakim D, Diem M. Infrared spectroscopy of human tissue II: A comparative study of spectra of biopsies of cervical squamous epithelium and of exfoliated cells. *Biospectroscopy* 1998;4:55-59.
11. McIntosh LM, Jackson M, Mantsch HH, Stranc MF, Pilavdzic D, Crowson AN. Infrared spectra of basal cell carcinomas are distinct from non-tumor-bearing skin components. *J Invest Dermatol* 1999;112:951-956.
12. Fukuyama Y, Yoshida S, Yanagisawa S, Shimizu MA. A study on the differences between oral squamous cell carcinomas and normal oral mucosas measured by Fourier transform infrared spectroscopy. *Biospectroscopy* 1999;5:117-126.
13. Liu KZ, Dixon IM, Mantsch HH. Distribution of collagen deposition in

- cardiomyopathic hamster hearts determined by infrared microscopy. *Cardiovasc Pathol* 1999;8:41–47.
14. Chiriboga L, Yee H, Diem M. Infrared spectroscopy of human cells and tissue VI: a comparative study of histopathology and infrared microspectroscopy of normal, cirrhotic, and cancerous liver tissue. *Appl Spectrosc* 2000;54:1–8.
  15. Yano K, Ohoshima S, Gotou Y, Kumaido K, Moriguchi T, Katayama H. Direct measurement of human lung cancerous and noncancerous tissues by Fourier transform infrared microscopy: can an infrared microscope be used as a clinical tool? *Anal Biochem* 2000;287:218–225.
  16. Kneipp J, Beekes M, Lasch P, Naumann D. Molecular changes of preclinical scrapie can be detected by infrared spectroscopy. *J Neurosci* 2002;22:2989–2997.
  17. Lewis EN, Treado PJ, Reeder RC, Story GM, Dowrey AE, Marcott C, Levin IR. Fourier transform spectroscopic imaging using an infrared focal-plane array detector. *Anal Chem* 1995;67:3377–3381.
  18. Kidder LH, Kalasinsky VF, Luke JL, Levin IW, Lewis EN. Visualization of silicone gel in human breast tissue using new infrared imaging spectroscopy. *Nat Med* 1997;3:235–237.
  19. Potter K, Kidder LH, Levin IW, Lewis EN, Spencer RGS. Imaging of collagen and proteoglycan in cartilage sections using Fourier transform infrared spectral imaging. *Arthritis Rheum* 2001;44:846–855.
  20. Camacho NP, West P, Torzilli PA, Mendelsohn R. FTIR Microscopic imaging of collagen and proteoglycan in bovine cartilage. *Biopolymers* 2001;62:1–8.
  21. Steiniger B, Barth P, Herbst B, Hartnell A, Crocker PR. The species-specific structure of microanatomical compartments in the human spleen: strongly sialoadhesin-positive macrophages occur in the perifollicular zone, but not in the marginal zone. *Immunology* 1997;92:307–316.
  22. Liu YJ, Barthelemy C, de Bouteiller O, Banchereau J. The differences in survival and phenotype between centroblasts and centrocytes. *Adv Exp Med Biol* 1994;355:213–218.
  23. Krafft C, Sobottka SB, Schackert G, Salzer R. Analysis of human brain tissue, brain tumors and tumors cells by infrared spectroscopic mapping. *Analyst* 2004;129:921–925.